Supporting Information

Ho et al. 10.1073/pnas.1403002111

SI Text

Wireless Power Transfer to Deep-Tissue Microimplants

Efficiency of Power Transfer. The expression for efficiency in the main text can be derived using coupled mode theory. In this formalism, the exchange of energy between the source and receiver is described by the equations

$$\dot{a}_S(t) = (i\omega_S - \Gamma_S)a_C(t) + \kappa a_S(t)$$

$$\dot{a}_C(t) = (i\omega_C - \Gamma_C - \Gamma_L)a_C(t) + \kappa a_S(t),$$

where a_n are amplitudes normalized such that $|a_n|^2$ corresponds to the energy in the structure, Γ_n the intrinsic decay rates, Γ_L the rate of work extraction by the load on the receiver, and κ the coupling coefficient. It is advantageous to operate with the source and receiver in resonance $\omega = \omega_S = \omega_C$ (1). The efficiency of power transfer is defined as

$$\eta' = \frac{\Gamma_L |a_S|^2}{\Gamma_S |a_S|^2 + (\Gamma_C + \Gamma_C)|a_S|^2 + \mathrm{Re}\left(\kappa a_S^* a_C\right)}.$$

In the limit of weak coupling $|\kappa|^2/\Gamma_S\Gamma_C \ll 1$, the expression reduces to

$$\eta' = \frac{|\kappa|^2}{\Gamma_S\Gamma_C} \frac{\Gamma_C/\Gamma_L}{(1+\Gamma_C/\Gamma_L)^2},$$

which is the product of two efficiencies (2). The left-hand factor can be understood as the efficiency of power transfer to the coil in absence of the load. The right-hand factor corresponds to the efficiency of power extraction by the load—this factor is maximized when the impedance-matching condition $\Gamma_C = \Gamma_L$ is satisfied. From standard power arguments, it can be shown that the left-hand efficiency is given by

$$\frac{|\kappa|^2}{\Gamma_S\Gamma_C} = \frac{\left| \int d^3r \ \mathbf{B}_S^* \cdot \mathbf{M}_C \right|^2}{\left[\int d^3r \, \mathrm{Im}\epsilon(\omega) |\mathbf{E}_S|^2 \right] \left[\int d^3r \, \mathrm{Im}\epsilon(\omega) |\mathbf{E}_C|^2 \right]}, \qquad \textbf{[S1]}$$

which is the efficiency in Eq. **S2**. Equivalent expressions can be obtained using other formalisms for coupled electrical systems, such as a two-port lumped element network (3).

Penetration of Time-Varying Fields in Tissue. Although electromagnetic waves varying in time at high frequencies (>100 MHz) are associated with high absorption in tissue, optimal transfer is found to occur in the low-gigahertz range. To understand this result, we consider the penetration of a plane wave $H_x(z,t) = H_0 \exp[i(kz - \omega t)]$ into a tissue half-space as the frequency ω varies. The depth at which the field extends into tissue is described by the skin depth $\delta := 1/\mathrm{Im}(k)$, where $k = \omega\sqrt{\mu\epsilon}$ is the wavenumber. Dispersion in tissue can be described by Debye relaxation $\epsilon/\epsilon_0 = \epsilon_\infty + \Delta\epsilon/(1 - i\omega\tau_D) + i\sigma/(\omega\epsilon_0)$, where σ is the conductivity, τ_D the characteristic relaxation time of the medium, ϵ_∞ the permittivity in the high-frequency limit, and $\Delta\epsilon := \epsilon_S - \epsilon_\infty$ (ϵ_S the static permittivity). The model is valid in the regime $\omega\tau_D \ll 1$, in which case the permittivity can also be approximated as

$$\epsilon/\epsilon_0 \approx \epsilon_S \left[1 + i\left(\omega\tau_D \frac{\Delta\epsilon}{\epsilon_S} + \frac{1}{\omega\tau_E} \right) \right], \qquad \textbf{[S2]}$$

where $\tau_E := \epsilon_0\epsilon_S/\sigma$ is the electric time constant. The relative significance of $\omega\tau_E$ and $1/\omega\tau_D$ determines the imaginary term's characteristic dependence on ω:

1. At low frequencies when $\omega\tau_E \ll 1$, the permittivity reduces to $\epsilon/\epsilon_0 \approx i\epsilon_S/\omega\tau_E$. The wavenumber is given by $k \approx \sqrt{\omega\mu_0\sigma/2}(1+i)$, from which one obtains the usual skin depth for conductors $\delta \approx \sqrt{2/\omega\mu_0\sigma}$.
2. When $\omega\tau_E \gg 1$ but $\omega\tau_E \ll 1/\omega\tau_D$, the τ_D term in Eq. **S2** can be neglected such that $\delta \approx 2\tau_E/\sqrt{\mu_0\epsilon_0\epsilon_S}$.
3. At high frequencies when $\omega\tau_E \gg 1/\omega\tau_D$, we approximate the permittivity as $\epsilon/\epsilon_0 \approx \epsilon_S(1 + i\omega\tau_D\Delta\epsilon/\epsilon_S)$. The skin depth is then given by $\delta \approx 2\epsilon_S/(\omega^2\tau_D\Delta\epsilon\sqrt{\mu_0\epsilon_0\epsilon_S})$.

The parameter $1/\tau_E$ and the geometric mean of $1/\tau_E$ and $1/\tau_D$ demarcate three frequency regimes

$$\delta \propto \begin{cases} 1/\sqrt{\omega}, & \omega \ll 1/\tau_E \\ \mathcal{O}(1), & 1/\tau_E \ll \omega \ll 1/\sqrt{\tau_D\tau_E} \\ 1/\omega^2, & \omega \gg 1/\sqrt{\tau_D\tau_E}. \end{cases}$$

Contrary to the notion that losses consistently increase with frequency, we find that there exists an intermediate range of frequencies across which the penetration is approximately constant. This behavior occurs when the typical time scale of an amplitude variation is much shorter than τ_E but substantially longer than τ_D. If one operates in this regime, the penetration is expected to be much greater than that naively extrapolated from a low-frequency conductor model of tissue. For the muscle tissue parameters, we calculate the range to be approximately between 690 MHz and 2.2 GHz, which is consistent with our implementation of midfield power transfer.

State-of-the Art Integrated Electronics. To illustrate the range of applications available with performance characteristics reported in the main text, Table S1 describes the power requirements of selected state-of-the-art integrated circuits (ICs). The table is not exhaustive, but is representative of existing solid-state circuit capabilities in the microwatt power regime. With the exception of ref. 4, all devices are currently powered with either wire tethers or large (>2 cm) near-field coils.

For stimulation, a local field-sensing IC was developed by Medtronic to enable closed-loop neurostimulation (5). As an alternative to electrical stimulation, an optogenetic stimulator consuming 400 μW was designed, with possibility of lower power with more efficient LEDs or opsins (6). A neural recording device consuming 0.73 μW per channel was demonstrated in ref. 7; less than 100 μW was required for 100-channel recording. A pacemaker IC, developed by St. Jude Medical, contains amplifiers, filters, analog-to-digital converters, battery management system, voltage multipliers, high-voltage pulse generators, programmable logic, and timing control, and consumes only 8 μW (8). A wide dynamic range bioimpedance sensor was also shown to extract QRS complex features for the detection of ventricular fibrillation (9).

ICs developed for monitoring physiological processes include a fluorometer for continuous glucose monitoring (10),

a cubic-millimeter intraocular pressure sensor (11), and a temperature sensor with an accuracy of ±0.15 °C (12). These sensors require energy in the range of nanojoules to microjoules per measurement. For imaging, a sensor consuming only 3.4 μJ per frame of 256 × 256 pixels with 8 bits per pixel has been demonstrated (13). An implantable device capable of locomotion in fluid has also been developed (4). Wireless communication allow remote control and noninvasive readout of these devices. In ref. 4, the data receiver consumes 0.5 pJ per bit. For the reverse link (from the device to the external source), the power consumption depends on the range, varying between picojoules to nanojoules per bit.

Safety Considerations. We refer to the Institute of Electrical and Electronics Engineers C95.3-2005 Standard (14) for general safety thresholds that are protective against all established adverse health effects. The basic metric for rf exposure is the specific absorption rate (SAR), defined as the power loss integral over a reference volume of tissue. Limits exist on the SAR induced by a source of electromagnetic fields to protect against adverse health effects arising from tissue heating. A system is compliant with the standard if (*i*) the whole-body average SAR is less than 0.4 W/kg and (*ii*) the maximum local SAR (averaged over 10 g of tissue) does not exceed 10 W/kg. These limits are reduced by a factor of 5 for general public exposure (uncontrolled environments), such as for cell phones.

Local SAR evaluation is more complicated because it involves estimating the spatial SAR distribution under realistic operating conditions. Following recommended procedures (15) within a compliance laboratory setting (Fig. S4), we measured the peak SAR point to be 2 W/kg for the body and 2.4 W/kg for the head when coupling 500 mW into tissue. Averaged over the specified 10 g of tissue, these values were found to be 0.89 W/kg and 1.17 W/kg, respectively, which are far below the specified limit (10 W/kg). Based on this data, the source power can be increased up to ∼4.2 W before the safety threshold is met.

Experimental results in the main text involve source power levels of 500 mW. These levels are clearly compliant to the whole-body average—the standard specifies that up to 28 W can be coupled into the body before exceeding the limit (14), when considering an average adult male (70 kg).

The millimeter-scale devices described in the main text consume very low levels of power (tens of microwatts) and are thus unlikely to pose direct safety concerns. Certain applications may require that the power be dissipated over extremely short timescales and/or concentrated in small volumes. Potential adverse effects should, in these cases, be considered in the context of the device's function and physiological environment.

1. Kurs A, et al. (2007) Wireless power transfer via strongly coupled magnetic resonances. *Science* 317(5834):83–86.
2. Kim S, Ho JS, Chen LY, Poon ASY (2012) Wireless power transfer to a cardiac implant. *Appl Phys Lett* 101:073701.
3. Ho JS, Kim S, Poon ASY (2013) Midfield wireless powering for implantable systems. *Proc IEEE* 101:1369–1378.
4. Yakovlev A, Pivonka D, Meng TH, Poon ASY (2012) A mm-sized wirelessly powered and remotely controlled locomotive implantable device. *IEEE ISSCC Dig Tech Papers*, 10.1109/ISSCC.2012.6177023.
5. Avestruz AT, et al. (2008) A 5 w/channel spectral analysis IC for chronic bidirectional brain–machine interfaces. *IEEE J Solid State Circuits* 43:3006–3024.
6. Paralikar K, et al. (2010) An implantable 5mW/channel dual-wavelength optogenetic stimulator for therapeutic neuromodulation research. *IEEE ISSCC Dig Tech Papers*, 10.1109/ISSCC.2010.5433938.
7. Han D, Zheng Y, Rajkumar R, Dawe G, Je M (2013) A 0.45V 100-channel neural-recording IC with sub-μW/channel consumption in 0.18 μm CMOS. *IEEE ISSCC Dig Tech Papers*, 10.1109/ISSCC.2013.6487739.
8. Wong LSY, et al. (2004) A very low-power CMOS mixed-signal IC for implantable pacemaker applications. *IEEE J Solid State Circuits* 39:2446–2456.
9. Kim S, et al. (2013) A 20 μW intra-cardiac signal-processing IC with 82 dB bio-impedance measurement dynamic range and analog feature extraction for ventricular fibrillation detection. *IEEE ISSCC Dig Tech Papers*, 10.1109/ISSCC.2013.6487745.
10. Dehennis AD, Mailand M, Grice D, Getzlaff S, Colvin AE (2013) A near-field-communication (NFC) enabled wireless fluorimeter for fully implantable biosensing applications. *IEEE ISSCC Dig Tech Papers*, 10.1109/ISSCC.2013.6487743.
11. Chen G, et al. (2011) A cubic-millimeter energy-autonomous wireless intraocular pressure monitor. *IEEE ISSCC Dig Tech Papers*, 10.1109/TCSI.2013.2265973.
12. Souri K, Chae Y, Makinwa K (2012) A CMOS temperature sensor with a voltage-calibrated inaccuracy of ±0.15° C (3σ) from 55 to 125° C. *IEEE ISSCC Dig Tech Papers*, 10.1109/JSSC.2012.2214831.
13. Choi J, Park S, Cho J, Yoon E (2013) A 3.4 μW CMOS image sensor with embedded feature-extraction algorithm for motion-triggered object-of-interest imaging. *IEEE ISSCC Dig Tech Papers*, 10.1109/JSSC.2013.2284350.
14. Institute of Electrical and Electronic Engineers (2005) *IEEE Standard for Safety Levels with Respect to Human Exposure to Radio Frequency Electromagnetic Fields, 3 kHz to 300 GHz* (IEEE, New York).
15. Institute of Electrical and Electronic Engineers (2005) *IEEE Recommended Practice for Determining the Peak Spatial-Average Specific Absorption Rate (SAR) in the Human Head from Wireless Communication Devices*. IEEE Standard 1528 (IEEE, New York).

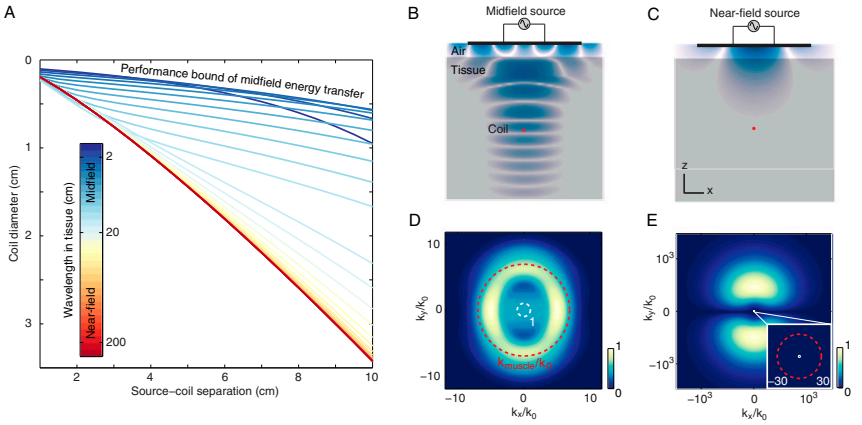

Fig. S1. Midfield and near-field power transfer comparison. (*A*) Performance curves (coil diameter vs. power transfer range) for fixed power-transfer efficiency $\eta = 10^{-3}$. To achieve this efficiency at a given wavelength (color bar), the coil size and operating depth is constrained to lie under the performance curve. The curves are generated by solving for optimal power transfer in an air–muscle half-space for the indicated depths and wavelength in tissue. (*B* and *C*) Optimal magnetic fields (time snapshot, H_y) corresponding to 5-cm separation in multilayers (tissue layers same as Fig. 1). The operating frequency is 1.6 GHz in *B* and 10 MHz in *C*. (*D*) Angular spectra of *B* at the source plane; (*E*) angular spectra of *C* at the source plane. k_0, wavenumber in air; k_{muscle}, wavenumber in muscle tissue. The separation between the source and tissue interface is 1 cm.

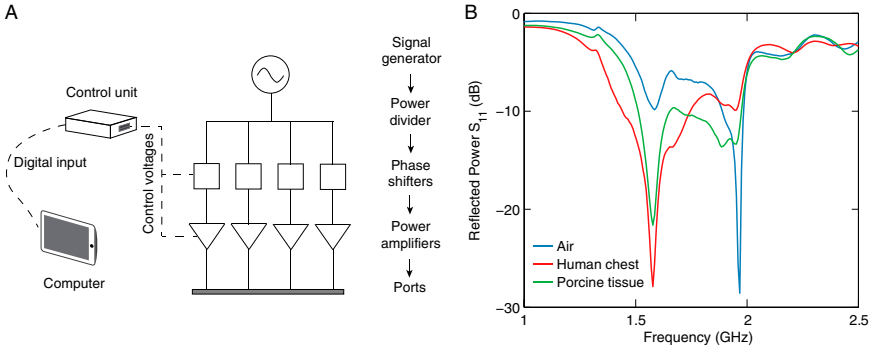

Fig. S2. Midfield source implementation. (*A*) Schematic of source components used to excite the metal plate and implement feedback-enabled control. (*B*) Scattering parameter (S_{11}) as a function of frequency, measured at an individual input port. When positioned 1 cm above the human chest or porcine tissue, the pronounced dip in the spectrum shifts to 1.6 GHz, indicating that power is efficiently coupled into tissue.

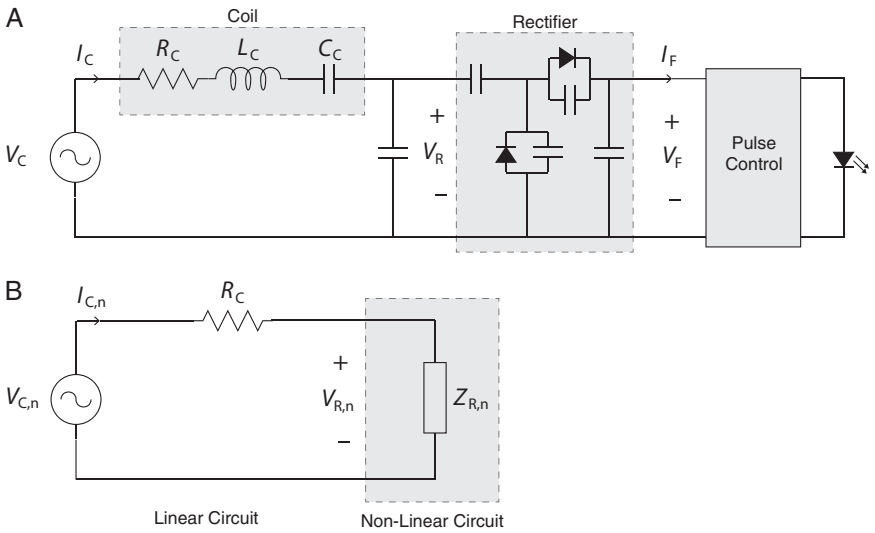

Fig. S3. Circuit schematic for the probe and pacemaker. (*A*) Lumped circuit model of the receiver. The AC voltage V_C generated across the coil by the source fields is converted to DC power through the rectifier circuitry. The power flowing through the pulse control circuitry is encoded in the flashing frequency of the LED. (*B*) Equivalent circuit at the *n*th reference power level when the circuit is at resonance. The nonlinear properties of the rectifier and pulse control unit enable the unknown parameter R_C to be estimated if the circuit is characterized at two reference flashing frequencies. Once the environment-dependent parameter R_C is known, the model enables the transferred power to be estimated.

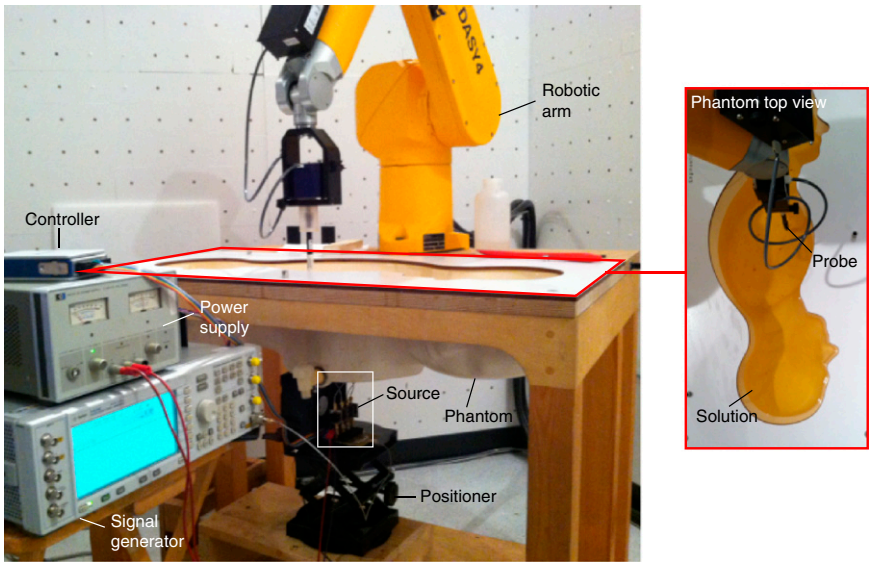

Fig. S4. SAR measurement setup. Photograph of the measurement setup used in the SAR measurements. The white box shows the location of the wireless powering source, and the red box the radiofrequency phantom filled with a body-simulating liquid. The robotic arm scans an electric field probe in the volume directly above the source during measurement.

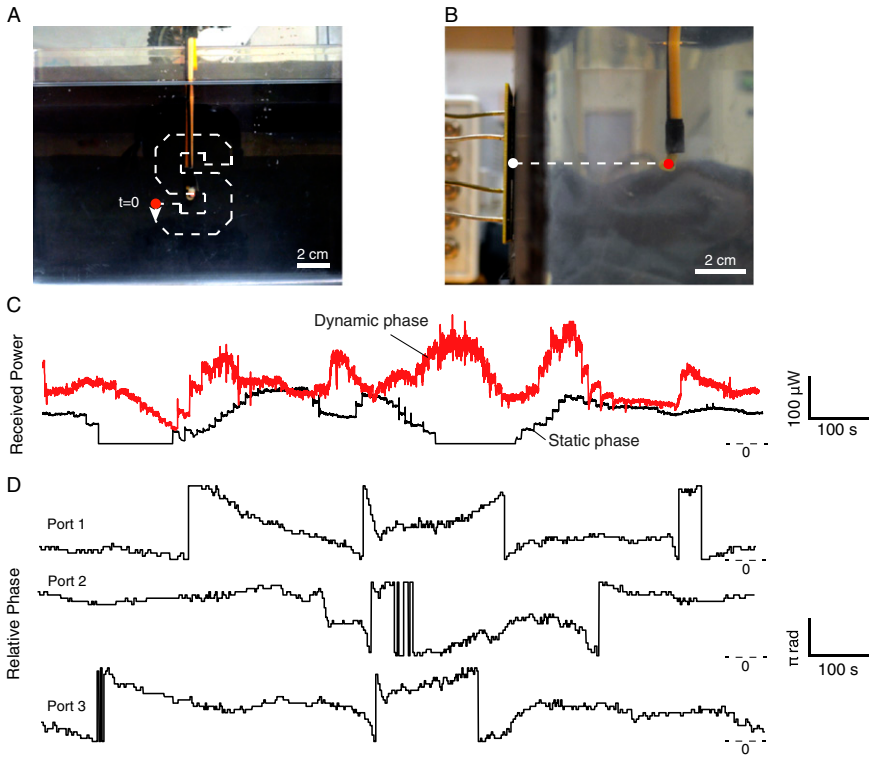

Fig. S5. Dynamic focusing for motion tracking. (*A*) Trajectory of the device in a liquid solution with dielectric properties imitating muscle tissue. The red dot marks the starting position. (*B*) Separation between the device (red dot) and the center of the source (white dot). The distance is ~6 cm, including a 1-cm air gap between the source and the liquid. (*C*) Power received by the device measured by the flashing rate of the LED. The minimum power to operate the device is ~10 μW. The dynamic phase adaptation algorithm enables higher levels of power to be transferred as the device moves. (*D*) Phase of each port, relative to a phase stationary port 4, controlled by the algorithm as the device is in motion.

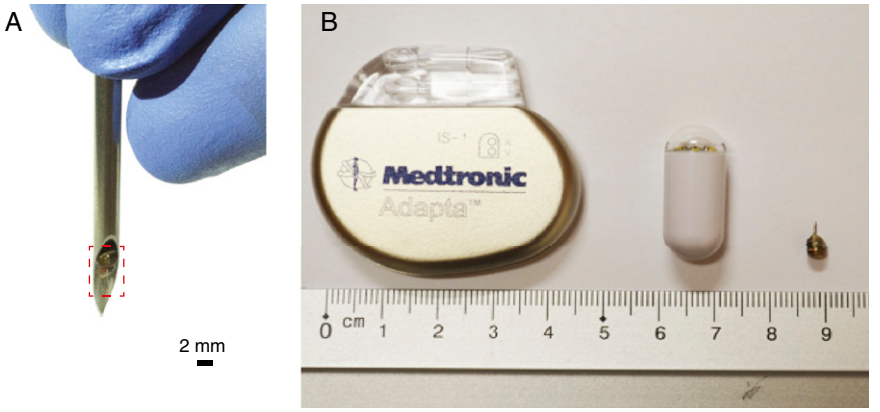

Fig. S6. Size comparison for the electrostimulation device. (*A*) Photograph of the electrostimulation device (red box), inserted in a 9-gauge (3 mm diameter) hypodermic needle for size comparison. (*B*) Device next to a conventional battery-powered pacemaker (*Left*; Medtronic Adapta), a battery-powered swallowable endoscope (*Center*), and the millimeter-scale pacing device (*Right*).

Table S1. Fabrication process and power consumption of selected integrated complementary metal-oxide-semiconductor (CMOS) electronics

Function	Fabrication process	Power consumption
Neural local field potential sensing (5)	0.8 μm CMOS	4.5 μW per channel
Optogenetic stimulation (6)	0.8 μm HV CMOS	400 μW
Neural recording (7)	0.18 μm CMOS	0.73 μW per channel
Pacemaker (8)	0.5 μm CMOS	8 μW
Intracardiac impedance measurement (9)	0.18 μm CMOS	6.67 μW per channel
Fluorometer (10)	0.6 μm CMOS	<1 μJ per measurement
Intraocular pressure sensor (11)	0.18 μm CMOS	1.44 μJ per measurement
Temperature sensor (12)	0.16 μm CMOS	0.027 μJ per measurement
CMOS image sensor (13)	0.18 μm CMOS	3.4 μJ per frame
Locomotion (4)	65 nm CMOS	250 μW at 0.53 cm/s